JOURNAL OF COMPUTATIONAL PHYSICS 78, 251–277 (1988)

The Alfvén Ion-Cyclotron Instability: Simulation Theory and Techniques

NIELS F. OTANI*

Electronics Research Laboratory, University of California, Berkeley. California 94720

Received September 22, 1986; revised August 7, 1987

The numerical properties of a particle-ion, fluid-electron computer simulation code, used in the study of the parallel-propagating electromagnetic Alfvén ion-cyclotron (AIC) instability, are examined. A numerical odd–even mode is suppressed by means of a two-timestep averaging method. Excellent energy conservation is obtained by using a method similar to the Boris particle mover to advance the transverse fields. Linear growth rates obtained from the code differ substantially from those predicted by uniform Vlasov theory, here derived using a multifluid model. Short wavelengths in particular show substantial growth rates when damping is predicted, and additionally show strong linear mode coupling. Positive growth rates are even observed in the case of a Maxwellian ion distribution. Disagreement is also generally found among short-wavelength mode frequencies. These inconsistencies are resolved by taking into consideration general grid and discrete-particle effects of the simulation model. A theoretical study reveals a real, physical process by which an ion distribution may collisionlessly relax via short-wavelength AIC instabilities acting resonantly on small portions of the distribution function. This process is combined with a linear mode coupling theory and other characteristics of the AIC instability to explain all observed differences. Nonlinear short-wavelength saturation levels are also obtained and their relevance to other field-aligned, electromagnetic simulations is discussed. © 1988 Academic Press, Inc.

I. INTRODUCTION

The Alfvén ion-cyclotron (AIC) instability is a plasma instability driven by free energy associated with an anisotropy in the ion velocity distribution function. Specifically, the instability requires the ion temperature perpendicular to a background magnetic field $\mathbf{B}_0$ to be greater than the ion parallel temperature ($T_{i\perp} > T_{i\parallel}$). The Alfvén ion-cyclotron instability is so called because it appears typically on that part of the dispersion curve which is intermediate between the shear Alfvén wave and the parallel-propagating ion-cyclotron wave. The AIC wave is thus typically thought of as traveling along $\mathbf{B}_0$ and indeed is usually the most unstable when propagating in that direction. Being on the Alfvén ion-cyclotron branch, the AIC instability is electromagnetic in nature, and for propagation along

* Present address: School of Electrical Engineering, Cornell University, Ithaca, New York 14853.

0021-9991/88 $3.00

Copyright © 1988 by Academic Press, Inc.
All rights of reproduction in any form reserved.

the field in a uniform plasma, is purely electromagnetic, with both electric and magnetic wave field vectors always pointing normal to $\mathbf{B}_0$.

Its existence was demonstrated recently in the tandem mirror experiment TMX at Livermore [1], and the possibility of its occurrence in other experimental fusion plasmas such as the theta-pinch [2] has been theorized. In the Livermore experiment, the anisotropy for the instability was produced by perpendicular heating of the end-plug ions induced by neutral beam injection oriented at an angle of 90° relative to the local magnetic field. The observed fluctuations had a frequency below that of the beta-depressed cyclotron frequency, had relatively low azimuthal mode structure, and had elliptically polarized wave magnetic field components—all characteristics expected of the AIC instability and inconsistent with the drift-cyclotron loss cone (DCLC) mode which had been seen in earlier mirror experiments. The instability has also been predicted to appear in certain axicell designs of the next-generation mirror experiment, MFTF-B [3].

Data from both ground-based and space-based detectors have suggested that the AIC instability may also occur in the Earth's magnetosphere. Recently, Mauk and McPherron [4] presented evidence collected from the geostationary satellite ATS-6 suggesting the instability may be operative on the daytime side on or near the Earth's geomagnetic equator. As argued by Cornwall *et al.* [5], the instability may also occur on the nighttime side during periods of particle injection into the ring current region from the magnetotail.

The AIC instability is similar in many respects to its electron analog, the whistler instability. The latter typically occurs at frequencies somewhat below the electron cyclotron frequency and is driven by the analogous anisotropy in the electron velocity distribution function. In a uniform plasma, individual modes of the AIC instability propagating along $\mathbf{B}_0$ rotate about $\mathbf{B}_0$ in the same sense that the ions gyrate; similarly, the wave field vectors associated with the whistler instability rotate in the electron gyrorotation direction.

Theoretical studies of the AIC instability have been conducted by many researchers. The first study of the instability appears to be due to Rosenbluth [6] and has since been analyzed by Sagdeev and Shafranov [7], Scharer *et al.* [8–10], Hasegawa [11], and others. Linear theory has been developed for the instability for ion velocity distributions occurring in mirror machines by G. R. Smith [12] and earlier by Cordey and Hastie [13] and Hanson and Ott [14]. The behavior of the instability in inhomogeneous plasmas has been examined by Rognlien [15], Watson *et al.* [16, 17], Tajima and Mima [18], and G. R. Smith *et al.* [3]. Characteristics of the AIC instability in the quasilinear regime have been studied by Sagdeev and Galeev [19] and Davidson and Ogden [2]. A theory presented by Ossakow, Ott, and Haber on the quasilinear saturation of the whistler instability [20] is also applicable to the AIC instability. References to further linear studies on the AIC instability in fusion plasmas and general plasmas appear in Ref. [12]; studies on the behavior of the instability in the space environment may be found in Refs. [4, 21].

The AIC instability has also been the subject of a number of simulation studies.

An early simulation study was carried out by Hasegawa and Birdsall [22] for $T_{i\perp} \neq 0$ and $T_{i\parallel} = 0$ in which rapid parallel heating of the ions was observed in the initial stages of the simulation and growth rates of the wave compared favorably with theory. Simulations involving both $T_{i\perp} \neq 0$ and $T_{i\parallel} \neq 0$ have been conducted for the AIC instability by Cuperman *et al.* [23], Tajima and Dawson [24], and Ambrosiano and Brecht [25], and for the whistler instability by Ossakow *et al.* [20]. All these simulations displayed initially rapid relaxation of the temperature anisotropy in the active species (ions for the AIC instability, electrons for the whistler instability) followed by a period of slower relaxation. A numerical, quasilinear study performed by Davidson and Ogden [2] also exhibited similar behavior. Mode coupling was observed in some of these simulations to transfer energy to the low wavenumber modes during the slow relaxation phase.

Although simulation techniques have been generally quite reliable in the study of the AIC instability, especially in the study of its nonlinear behavior, difficulties have been encountered. Systems initialized with zero-current equilibria (i.e., quiet-start simulations,) often exhibit linear growth rates substantially higher than those predicted by theory. This is especially true of the high wavenumber modes. Positive growth rates are even observed in the simulation of a Maxwellian ion distribution which of course is theoretically stable. The linear simulations of Byers *et al.* [26, 27] demonstrate that carefully chosen methods can circumvent the problem; nevertheless, investigation of the underlying causes of these growth rates is still useful, since it exposes much of the nature of simulations of this type. The saturation levels of these modes is also of concern. If the levels are higher than the amplitudes of the physical effects being studied, results of the simulation become meaningless.

These difficulties and related simulation characteristics are the subject of this study. The results obtained here apply not only to the simulation of the AIC instability, but to simulations involving parallel-propagating electromagnetic waves in the ion-cyclotron frequency range in general. Some of the results also apply to higher frequency regimes, including the electron cyclotron frequency regime. The general simulation characteristics described do not depend on the specific algorithm used; any simulation using ion particles and a spatial grid incorporating the same general physics should display similar characteristics.

The results presented here also serve as a case study for particle simulations in general, and electromagnetic particle simulations of parallel wave propagation in particular. The usual discrete-particle and nonphysical grid-aliasing effects assume new guises in these systems producing different and interesting new behavior. This behavior is of potential importance to many kinds of simulations, since the possibility always exists that these effects will interfere with the evolution of the physical effects under study. Additionally, one of the mechanisms described, the "one-beam" AIC instability, is itself a physical effect of some interest, as it provides another pathway for free energy in a particle velocity distribution to collisionlessly relax apart from the bump-on-tail instablity.

II. The AIC Linear Dispersion Relation

The linear dispersion relation appropriate to the Alfvén ion-cyclotron (AIC) instability is well known for propagation of the wave along the background magnetic field $B_0\hat{\mathbf{z}}$ in a uniform plasma [2, 10, etc.]. Here we again derive the AIC dispersion relation but use a "multifluid" model instead of the usual Vlasov equation as the basis for the calculation. The advantage of this approach lies in its conceptual simplicity—one observes the direct connection between features of the wave responsible for producing the various linear currents and terms in the dispersion relation.

By considering the ion phase space fluid in the Vlasov description to be composed of an uncountably infinite number of cold fluids, each with its own characteristic set of zero-order quantities v_z, $v_\perp$, and gyrophase θ at time t, we may write the perturbed transverse ion current in, say, the $\hat{\mathbf{y}}$-direction as

$$(J_i)_{y1}(z, t) = e\int dv_z\, v_\perp\, dv_\perp f^0(v_z, v_\perp) \int d\theta [n_0\, v_{y1}(v_z, z, t) + n_1(v_z, v_\perp, \theta, z, t)\, v_y], \quad (1)$$

where the ion velocity distribution function, $f^0(v_z, v_\perp)$, is normalized according to

$$\int d\theta\, dv_z v_\perp\, dv_\perp f^0(v_z, v_\perp) = 1, \quad (2)$$

n_0 is the unperturbed ion density, $v_y = v_\perp \cos\theta$, and $d\theta\, dv_z v_\perp\, dv_\perp f^0 n_1(v_z, v_\perp, \theta, z, t)$ and $v_{y1}(v_z, z, t)$ are respectively the perturbation density and perturbation $\hat{\mathbf{y}}$-velocity of the cold fluid element with zero-order quantities $v_z, v_\perp, \theta$, and z at time t. The perturbation density n_1 in Eq. (1) may be expressed as

$$n_1(v_z, v_\perp, \theta, z, t) = -n_0 \frac{\partial}{\partial z} z_1(v_z, v_\perp, \theta, z, t). \quad (3)$$

Assume the perturbation wave field takes the form of a single, purely transverse, circularly polarized, sinusoidal wave of wavenumber k and frequency ω propagating in the direction of the uniform magnetic field $B_0\hat{\mathbf{z}}$. The required components of the perturbed ion motion in these fields are easily found to be (real part implied):

$$v_{y1}(t) = \frac{eB_1}{kmc} \frac{\omega - kv_{z0}}{\omega - kv_{z0} - \Omega} \exp(ikz_0(t) - i\omega t) \quad (4)$$

and

$$z_1(t) = -\frac{eB_1/mc}{(\omega - kv_{z0} - \Omega)^2} (v_{x0}(t) - iv_{y0}(t)) \exp(ikz_0(t) - i\omega t), \quad (5)$$

where $\Omega \equiv \omega_{ci} \equiv eB_0/mc$, m is the *ion* mass, and the 0-subscripted quantities represent the unperturbed magnetized ion motion. The electrons may be assumed

to be a cold fluid, drifting in response to the perturbation transverse electric field with the $\mathbf{E}\times\mathbf{B}$ velocity:

$$(J_e)_{y1} = -\frac{en_0 c(\mathbf{E}_1\times\mathbf{B}_0)_y}{B_0^2}. \tag{6}$$

Substituting Eqs. (3), (4), and (5) into Eq. (1) and applying Ampère's law,

$$0 = \frac{c}{4\pi}\nabla\times\mathbf{B} - (J_e)_{y1} - (J_i)_{y1}, \tag{7}$$

then yields the AIC dispersion relation

$$0 = \frac{k^2 v_A^2}{\Omega^2} + \frac{\omega}{\Omega} + \int dv_z\, dv_\perp f^0(v_z, v_\perp)\left(\frac{\omega - kv_z}{\omega - kv_z - \Omega} + \frac{(1/2)\,k^2 v_\perp^2}{(\omega - kv_z - \Omega)^2}\right), \tag{8}$$

where $v_A \equiv B_0/(4\pi m n_0)^{1/2}$ is the Alfvén velocity.

The first term is the free-space term and the second term is the electron $\mathbf{E}\times\mathbf{B}$ contribution. From the infinite fluid derivation, we know the third term comes from the $n_0 v_{y1}$ term in Eq. (1) and thus results from the perturbed transverse ion motion, while the fourth term arises from the transverse ion current generated by the inhomogeneous first-order displacements of ions along $\mathbf{B}_0$, which we deduce by considering the effect of the spatial derivative in Eq. (3) on the form of Eq. (5). The current appears because the different fluids, with different zero-order transverse velocities, experience different differential displacements, and therefore contribute with differing densities to the transverse current density at a given location z. It is this last term which is responsible for the AIC instability.

III. The Simulation Algorithm

The main code used for the simulations presented in this study, TRACY (transverse AIC simulation), is a one-dimensional, spatially periodic code using a spatial grid along the direction of a static, uniform, unperturbed magnetic field $B_0\hat{\mathbf{z}}$. TRACY follows the one spatial coordinate z and all three velocity components of particle ions moving self-consistently in the transverse electric and magnetic fields. Electrons are treated as a linear $\mathbf{E}\times\mathbf{B}$ fluid.

The algorithm begins each timestep by updating ion velocities using a standard Boris mover scheme [28];

$$\mathbf{v}_i^a = \mathbf{v}_i^{t-1/2} + \frac{1}{2}\sum_j S(z_j - z_i^t)\,\mathbf{E}_j^t, \tag{9}$$

$$\mathbf{v}_i^b = \mathbf{v}_i^a + \frac{1}{2}\sum_j S(z_j - z_i^t)\,\mathbf{v}_i^a\times\mathbf{B}_j^t, \tag{10}$$

$$\mathbf{v}_i^c = \mathbf{v}_i^a + \sum_j S(z_j - z_i^t)\, \mathbf{v}_i^b \times \frac{\mathbf{B}_j^t}{1 + 0.25\,|\mathbf{B}_j^t|^2}, \tag{11}$$

$$\mathbf{v}_i^{t+1/2} = \mathbf{v}_i^c + \frac{1}{2} \sum_j S(z_j - z_i^t)\, \mathbf{E}_j^t. \tag{12}$$

Here i is the particle index, j is the grid index, t is the timestep index, and S is the particle-in-cell shape factor [29]. Computer variables with normalizations $\mathbf{v} \to \mathbf{v}/v_A$, $z \to z/(v_A\, \Delta t)$, $\mathbf{E} \to e\mathbf{E}\, \Delta t/mv_A$, $\mathbf{B} \to e\mathbf{B}\, \Delta t/mc$, $\mathbf{J}_{\text{ion}} \to (N/N_g)(J_{\text{ion}}/en_0 v_A)$, and $\mathbf{A} \to e\mathbf{A}\, \Delta t/mc\, \Delta z$ are used in the algorithm, where N_g is the number of grid points in the system, N is the number of particles in the system, and Δt and Δz are the timestep and grid spacing, respectively. The ion positions are next advanced one-half timestep:

$$z_i^{t+1/2} = z_i^t + \tfrac{1}{2}(v_z)_i^{t+1/2}. \tag{13}$$

Next, ion currents are collected at the grid points:

$$(\mathbf{J}_{\text{ion}})_j^{t+1/2} = \sum_i S(z_j - z_i^{t+1/2})\, \mathbf{v}_i^{t+1/2}, \tag{14}$$

and $\mathbf{J}_{\text{ion}}^{t+1/2}$ and the vector potential $\mathbf{A}^t$ are transformed to Fourier space. Here $\mathbf{A}$ is defined so that $\partial \mathbf{A}/\partial t = -c\mathbf{E}$ and $\nabla \times \mathbf{A} = \mathbf{B}_\perp$ as $\Delta t, \Delta z \to 0$. Since electrons are being treated as a linear $\mathbf{E} \times \mathbf{B}$ fluid and since displacement current is being neglected, Ampère's law takes the form

$$\frac{4\pi n_0 e}{c} \frac{\partial \tilde{\mathbf{A}}}{\partial t} \times \frac{\mathbf{B}}{B^2} = k^2 \tilde{\mathbf{A}}(k, t) - \frac{4\pi}{c} \tilde{\mathbf{J}}_{\text{ion}}(k, t). \tag{15}$$

The similarity of this equation to

$$\frac{d\mathbf{v}}{dt} = \frac{e}{m} \mathbf{E} + e\, \frac{\mathbf{v} \times \mathbf{B}}{mc}, \tag{16}$$

suggests we again make use of the Boris scheme:

$$\tilde{\mathbf{A}}_k^a = \tilde{\mathbf{A}}_k^t + \frac{1}{2} v_A \omega_{cu} \frac{\Delta t^2}{\Delta z} \frac{N_g}{N} (\mathbf{J}_{\text{ion}})_k^{t+1/2} \times \hat{\mathbf{z}}, \tag{17}$$

$$\tilde{\mathbf{A}}_k^b = \tilde{\mathbf{A}}_k^a + \frac{1}{2} \tilde{\mathbf{A}}_k^a \times \mathbf{b}_k, \tag{18}$$

$$\tilde{\mathbf{A}}_k^c = \tilde{\mathbf{A}}_k^a + \tilde{\mathbf{A}}_k^b \times \frac{\mathbf{b}_k}{1 + 0.25\,|\mathbf{b}_k|^2}, \tag{19}$$

$$\tilde{\mathbf{A}}_k^{t+1} = \tilde{\mathbf{A}}_k^c + \frac{1}{2} v_A \omega_{ci} \frac{\Delta t^2}{\Delta z} \frac{N_g}{N} (\mathbf{J}_{\text{ion}})_k^{t+1/2} \times \hat{\mathbf{z}}, \tag{20}$$

where

$$\mathbf{b}_k \equiv -\hat{\mathbf{z}} \frac{k^2 v_A^2}{\omega_{ci}} \Delta t. \tag{21}$$

Note that in this one-dimensional transverse system, only transverse components of **A** need be computed. This scheme has the natural advantage of conserving the magnitude of **A** in the absence of $\mathbf{J}_{\text{ion}}$, a desirable feature in view of Eq. (15). With both field and particle equations being advanced by Boris-like movers, we expect above-average energy conservation properties, and indeed, the quantity

$$\sum_i \frac{m v_i^2}{2} + \int \frac{B_{\text{wave}}^2}{8\pi} dz \tag{22}$$

is typically conserved to better than 3 parts in 10^4 in simulations presented in this study.

The new magnetic field is obtained next from

$$(\mathbf{B}_k^s)^{t+1} = k\, \Delta z (\tilde{\mathbf{A}}_k^c)^{t+1} \times \hat{\mathbf{z}}, \tag{23}$$

$$(\tilde{\mathbf{B}}_k^c)^{t+1} = -k\, \Delta z (\tilde{\mathbf{A}}_k^s)^{t+1} \times \hat{\mathbf{z}}, \tag{24}$$

where the superscripts s and c stand for the sine and cosine components, respectively. After inverse-Fourier transforming $\mathbf{B}^{t+1}$ and $\mathbf{A}^{t+1}$, the new electric field is obtained from

$$\frac{\mathbf{E}_j^{t+1} + \mathbf{E}_j^t}{2} = -\frac{\Delta z}{v_A\, \Delta t} (\mathbf{A}_j^{t+1} - \mathbf{A}_j^t). \tag{25}$$

Finally, particle positions are advanced another half timestep:

$$z_i^{t+1} = z_i^{t+1/2} + \tfrac{1}{2} (v_z)_i^{t+1/2}, \tag{26}$$

completing the timestep loop.

Following the method presented in, for example, Ref. [30], a dispersion relation has been found for this algorithm for the case of a cold, uniform ion distribution:

$$0 = \frac{k^2 v_A^2}{\omega_{ci}^2} \pm \frac{\tan \dfrac{\omega\, \Delta t}{2}}{\dfrac{\omega_{ci}\, \Delta t}{2}} + \frac{\sin^4 \dfrac{k\, \Delta z}{2}}{\left(\dfrac{k\, \Delta z}{2}\right)^4} \frac{\tan \dfrac{\omega\, \Delta t}{2} \left(1 + \tan^2 \dfrac{\omega\, \Delta t}{2}\right)}{\tan \dfrac{\omega\, \Delta t}{2} \mp \dfrac{\omega_{ci}\, \Delta t}{2}}. \tag{27}$$

Qualitative features of the roots are shown in Fig. 1. In addition to the expected electron-cyclotron and ion-cyclotron branches, a third branch appears at very high frequency ($\omega\, \Delta t \approx \pi$). We see this odd–even mode is stable for $v_A\, \Delta t / \Delta z$ appreciably less than 1 (the Courant limit) but is nevertheless a nuisance. For $v_A\, \Delta t / \Delta z \geqslant 1$, the algorithm becomes unstable as the odd–even mode interacts with the electron-cyclotron branch.

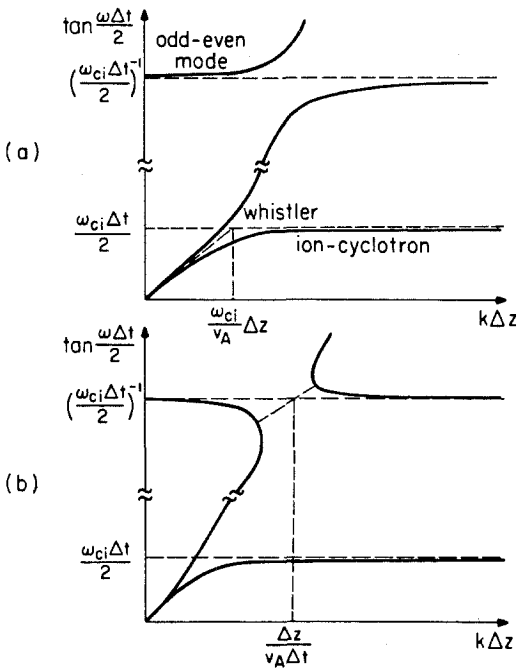

FIG. 1. Numerical dispersion relations for Eq. (27) for the cases (a) $v_A \Delta t/\Delta z \lesssim 1$ and (b) $v_A \Delta t/\Delta z \gtrsim 1$.

A reasonable cure for the stable odd–even mode has been found in the form of "two-timestep averaging" of the electric field and vector potential. This is implemented by solving for **A** and **E** as

$$\mathbf{A}_j^{\text{avg}} = \frac{1}{2}(\mathbf{A}_j^{t+1} + \mathbf{A}_j^t), \tag{28}$$

$$\mathbf{E}_j^{\text{avg}} = -\frac{\Delta z}{v_A \Delta t}(\mathbf{A}_j^{\text{avg}} - \mathbf{A}_j^t), \tag{29}$$

and now we take these averaged quantities to be the field quantities at timestep $t+1$. Since the odd–even mode frequency is such that $\omega_{\text{oe}} \Delta t \approx \pi$ while the physical phenomena we wish to recover have $\omega \Delta t \ll \pi$, two-timestep averaging kills the odd–even mode while having minimal effect on the physics. The effect of this procedure is illustrated in Fig. 2. The two runs shown in Fig. 2 are identical except that two-timestep averaging was performed *once* in the run illustrated in Fig. 2(b). The odd–even mode has never been observed to reappear following the averaging, demonstrating its effectiveness. In the standard version of the code, two-timestep averaging takes place once only using the first two timesteps.

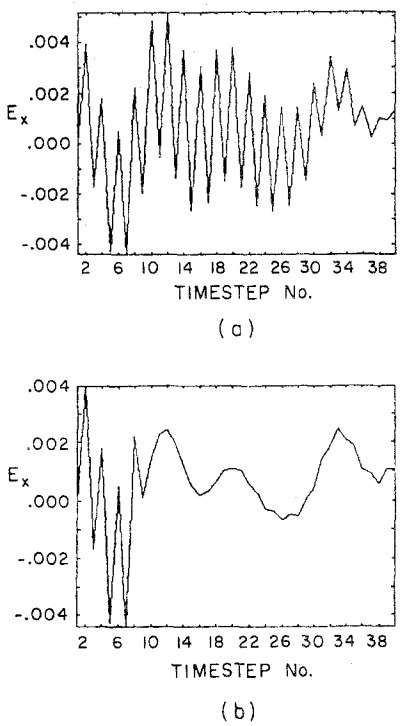

FIG 2. Electric field histories (x-component) for the first 40 timesteps for (a) a run not using two-timestep averaging, and (b) a run using two-timestep averaging of timesteps 8 and 9.

IV. THE ONE-BEAM AIC INSTABILITY

Many of the features observed in simulations of the linear regime of the AIC instability are most easily studied by using as the initial ion distribution a non-physical "multibeam" distribution function of the form

$$f^0(\mathbf{v}, z) = \frac{1}{N_b N_i v_\perp} \sum_{b=0}^{N_b-1} \delta(v_\perp - v_{\perp b})\, \delta(v_z - v_{zb}) \sum_{i=1}^{N_i} \delta(z - z_{ib})\, \delta(\theta - \theta_{ib}), \quad (30)$$

where $v_{\perp b}$ and v_{zb} are the perpendicular and parallel velocities associated with a given beam b, and z_{ib} and θ_{ib}, $i = 1, ..., N_i$ define the spatial and gyrophase coordinates represented by particles in that beam. The use of such a distribution function has two advantages: (1) the linear behavior of this distribution in simulation is more accessible to theoretical analysis than is, say, the bimaxwellian distribution, and (2) this distribution has comparatively few distinct values of $v_\perp$ and $v_\parallel$, allowing each $(v_\perp, v_\parallel)$ pair to be initially loaded uniformly along the spatial grid of the system. The latter allows for cleaner simulation diagnostics, and of course is a factor in simplifying the analysis.

Consider then the linear growth rates and frequencies that would be expected of the multibeam distribution. First assume each $(v_\perp, v_\parallel)$ pair, i.e., each beam b is loaded uniformly in both physical space and gyrophase space. Then

$$f^0(v) = \frac{1}{2\pi v_\perp N_b} \sum_{b=0}^{N_b-1} \delta(v_\perp - v_{\perp b})\, \delta(v_z - v_{zb}), \tag{31}$$

where N_b is the number of beams. From the general form of the AIC dispersion relation given by Eq. (8), we easily obtain the relevant dispersion relation:

$$0 = \frac{\omega}{\Omega} + \frac{k^2 v_A^2}{\Omega^2} + \frac{1}{N_b} \sum_{b=0}^{N_b-1} \left(\frac{\omega - k v_{zb}}{\omega - k v_{zb} - \Omega} + \frac{(1/2)\, k^2 v_{\perp b}^2}{(\omega - k v_{zb} - \Omega)^2} \right). \tag{32}$$

Equation (32) has been numerically solved for ω. A typical spectrum of solutions for the multibeam distribution is shown in Fig. 3. The beam parallel velocities were calculated to represent a Maxwellian distribution. A similar spectrum for the physically more realistic bimaxwellian ion distribution having the same values of $T_{i\perp}$ and $T_{i\parallel}$ is also plotted for comparison.

The agreement between the two spectra is good at long wavelengths ($k \lesssim O(\Omega/v_A)$). However, in the high-k portion of the spectrum, decidedly different

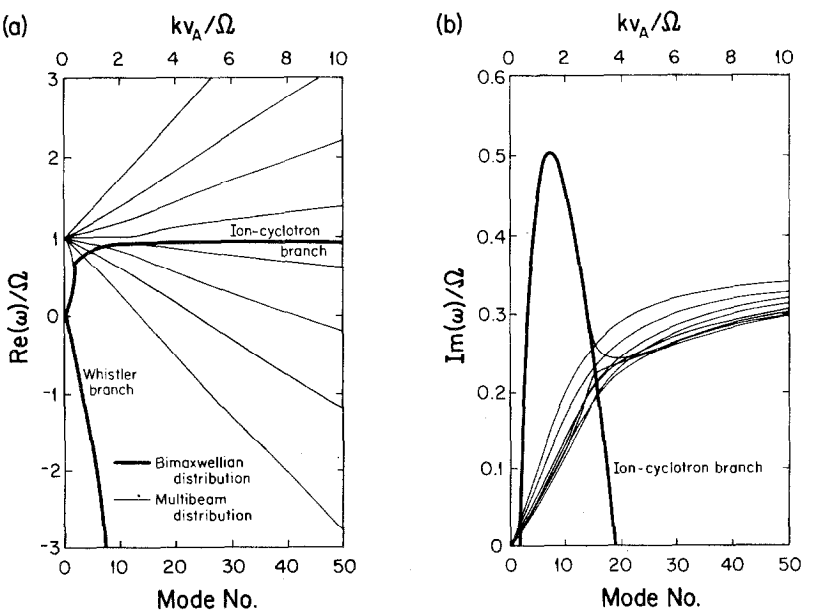

FIG. 3. (a) Linear frequencies and (b) linear growth rates vs wavenumber for bimaxwellian and 8-beam multibeam ion distribution functions having $\beta_{i\perp} = 2$ and $T_{i\perp}/T_{i\parallel} = 16$.

behavior is exhibited by the multibeam distribution. We can explain this behavior in terms of "one-beam" AIC instabilities. That is, for high enough k, it is possible for the ion response to be dominated by a single beam in the ion distribution function. The resonant beam has infinite temperature anisotropy ($T_{i\perp}/T_{i\parallel} = \infty$), whenever its perpendicular velocity $v_{\perp b}$ is non-zero, and is therefore capable of driving the instability.

Assume the mode frequency associated with the resonant beam, say, the beam $b = 0$ in Eq. (31), is expressible as

$$\omega_d \equiv \omega_{d0} + \frac{\omega_{d1}}{k} + \frac{\omega_{d2}}{k^2} + O(k^{-3}) \qquad \text{as} \quad k \to \infty, \tag{33}$$

where $\omega_d \equiv \omega - kv_{z0} - \Omega$ is the deviation of the mode frequency from the Doppler-shifted ion-cyclotron frequency, and ω_{d0}, ω_{d1}, and ω_{d2} are independent of k. We find that Eq. (32) may be expanded consistently with Eq. (33) to yield

$$\omega_{d0} = \pm \frac{i\Omega v_{\perp 0}}{\sqrt{2N_b}\, v_A}, \tag{34}$$

$$\frac{\omega_{d1}}{k} = \mp \frac{i\Omega}{2\sqrt{2N_b}} \left(\frac{\Omega}{kv_A}\right) \frac{v_{z0} v_{\perp 0}}{v_A^2}, \tag{35}$$

and

$$\frac{\omega_{d2}}{k^2} = \frac{\Omega v_{\perp 0}}{2\sqrt{2N_b} v_A} \left(\frac{\Omega}{kv_A}\right)^2 \left\{ \frac{1}{\sqrt{N_b}} \left(\frac{v_{\perp 0}}{\sqrt{2} v_A} - \frac{\sqrt{2} v_A}{v_{\perp 0}} \right) \right.$$
$$\left. \pm i \left[\frac{3}{4} \left(\frac{v_{z0}}{v_A} \right)^2 - 2 - \frac{1}{N_b} \sum_{b=1}^{N_b - 1} \frac{(1/2)\, v_{\perp b}^2}{(v_{z0} - v_{zb})^2} \right] \right\}. \tag{36}$$

For large enough k, the ω_{d0} term dominates in Eq. (33) and we recover as the imaginary part of the frequency just the infinite-anisotropy AIC growth rate for that beam (Eq. (34)). Numerical evaluation of the roots of Eq. (32) verifies this; as $k \to \infty$, the calculated linear growth rates are observed to approach the values predicted by Eq. (34) (Fig. 4). The expression for ω_{d0} is pure imaginary, implying that the real part of the mode frequency is the Doppler-shifted ion cyclotron frequency, $\Omega + kv_{z0}$, to zero order. We also note that the $k \to \infty$ asymptotic growth rate scales as $1/\sqrt{N_b}$. These are just the characteristics expected of the AIC instability of a single, infinitely anisotropic distribution having the density and parallel velocity of the ($b = 0$)-beam.

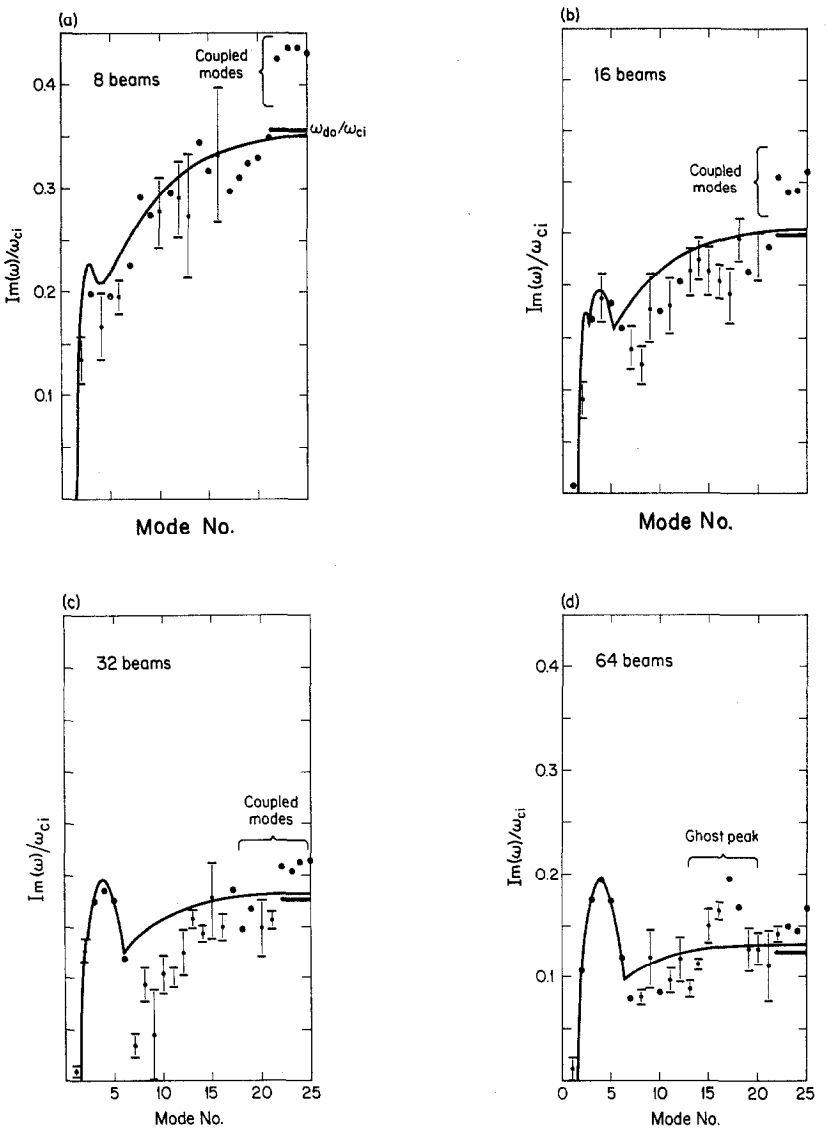

FIG. 4. Theoretical and simulated maximum growth rates vs mode number for multibeam ion distribution functions composed of (a) 8 beams, (b) 16 beams, (c) 32 beams, (d) 64 beams, and (e) 128 beams with $\beta_{i\perp}=2$ and $T_{i\perp}/T_{i\parallel}=4$. The theoretical asymptotic ($k\to\infty$) growth rates ω_{d0}/w_{ci} is also indicated (heavy horizontal bars). Each of the beams is composed of 47 groups of particles each containing four particles initially arranged $\pi/2$ apart in gyrophase space. The simulations retained modes -25 to 25 with $kv_A/\omega_{ci}=0.199\times$ (mode number).

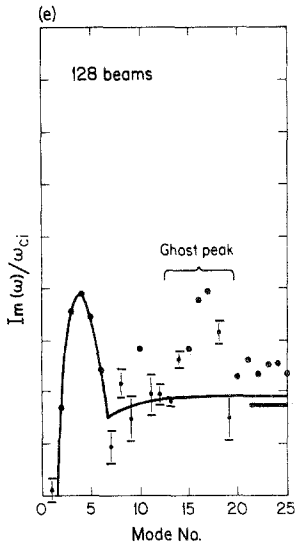

FIGURE 4 *(continued)*

V. LINEAR MODE COUPLING

Simulations using the multibeam distribution function with various numbers of beams show excellent agreement with both the frequencies and growth rates obtained at long wavelengths from the numerical solution of Eq. (32), as shown in Figs. 4 and 5(a). The observed short-wavelength growth rates and frequencies also generally agree, but there are notable exceptions. The shortest wavelengths followed by the simulations often exhibit growth rates substantially larger than those predicted by theory (modes 22–25 in Figs. 4(a) through 4(c)). Additional peaks ("ghost peaks") sometimes appear in the growth spectrum (Figs. 4(d) and (e)). Finally, a strong whistler frequency component often accompanies the one-beam AIC mode(s) at short wavelengths (Fig. 5). The whistler component grows as rapidly as the fastest growing one-beam mode, even though Eq. (32) predicts the whistler to be stable.

All of these discrepancies may be explained by considering the combined effects of grid aliasing and linear mode coupling in the simulations. Mode coupling, or the transfer of energy from a wave at one wavelength to other wavelengths, can only occur in the linear regime when spatial non-uniformities are present in the equilibrium. In the present case, the non-uniformities are found in the spatial ion distribution as a consequence of our use of particle ions and enter the equations through the linearized source terms. In the case of our AIC simulations, the relevant source term is the linearized transverse ion current. The essence of the linear coupling is thus easily understood. The linear current response of ions to a

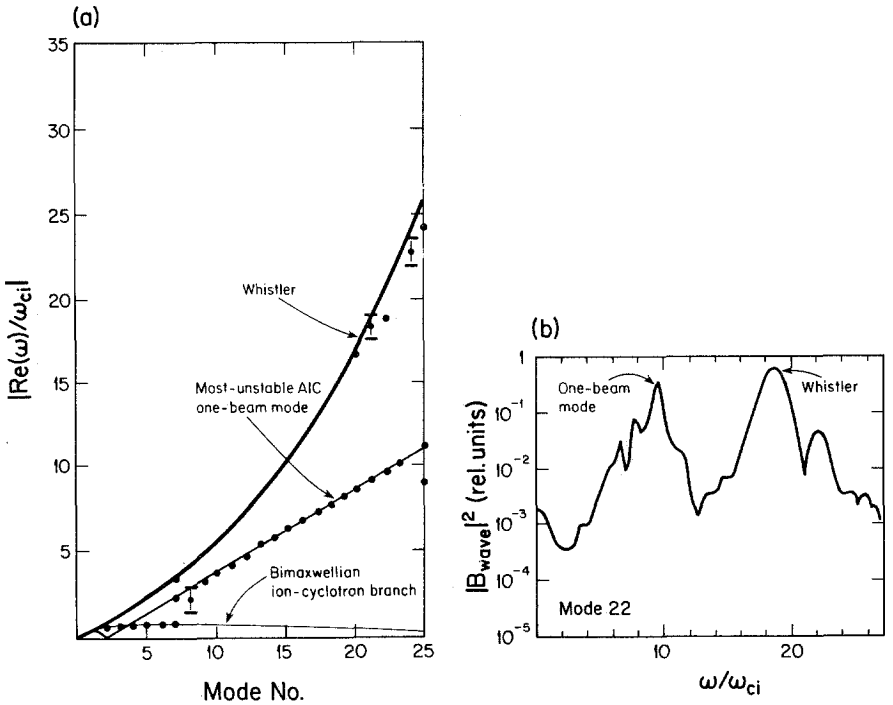

FIG. 5. (a) Principal linear frequencies vs. mode number of a 64-beam multibeam simulation with $\beta_{i\perp}=8$, $T_{i\perp}/T_{i\parallel}=4$, and $kv_A/\omega_{ci}=0.199\times$(mode number). Selected theoretical linear dispersion curves are also plotted for comparison. (b) A typical frequency spectrum from the linear phase of the simulation.

transverse wave at a given wavelength will not be entirely at that wavelength because the constituent linear particle currents are not uniformly distributed in space. The coupling mechanism may also be described as wave-particle scattering or, in the case of regularly spaced particles (as is the case in our multibeam simulations), "particle-grid" aliasing.

The equations required for describing these effects are derived by substituting linear expressions for $\delta\mathbf{v}_{is}$ and δz_{is} into components of the linearized expression for the transverse current,

$$\mathbf{J}_j(t)=\frac{n_0 eN_g}{N}\sum_i\left[S(z_i^0(t)-z_j)\sum_s\delta\mathbf{v}_{is}(t)+S'(z_i^0(t)-z_j)\sum_s\mathbf{v}_{is}^0(t)\,\delta z_{is}(t)\right]$$
$$+\frac{n_0 e}{B_0^2}\frac{\partial\mathbf{A}_j}{\partial t}\times\mathbf{B}_0, \tag{37}$$

where i indexes particle "groups," s labels the particles in each such group, N is the total number of particles, $z_i^0(t)=z_i^0+v_\parallel^0 t$, $\mathbf{v}_{is}^0(t)=\hat{\mathbf{x}}v_{i\perp}^0\sin(\theta_{is}^0+\Omega t)+$

$\hat{\mathbf{y}} v_{i\perp}^0 \cos(\theta_{is}^0 + \Omega t)$ are the perpendicular zero-order trajectories, $S(z)$ is the shape factor of each particle, and z_j is the z-position of grid-point j. Here $\delta \mathbf{v}_{is}(t)$ and $\delta z_{is}(t)$ are the linear perturbed quantities for particle s in group i, and $\mathbf{A}_j$ is the perturbed vector potential at grid j. A particle "group" here refers to a group of particles all having the same initial, zero-order values of $v_\parallel$, $v_\perp$, and z. In our simulations particles were loaded in groups of four at intervals of $\pi/2$ in gyrophase space, with the first gyrophase angle chosen at random. This "four-spokes" gyrophase distribution maintains a constant perpendicular velocity second moment in the absence of wave fields while minimizing the number of particles required to represent realistic ion distribution functions. It can be shown that the only aspect of the perpendicular distribution participating in the linear physics is the second moment. Also, quiet starts are possible with the four-spokes distribution, since there is no associated transverse current. Again, ions are represented as particles while electrons enter only through the electron $\mathbf{E} \times \mathbf{B}_0$ current. In this calculation we ignore the finite timestep size Δt.

Expressions for $\delta \mathbf{v}_{is}(t)$ and $\delta z_{is}(t)$ in the ion terms in Eq. (37) may be calculated from the linearized ion equation of motion

$$\frac{d}{dt}\delta \mathbf{v}_{is} + \boldsymbol{\Omega} \times \delta \mathbf{v}_{is} = \frac{e}{m} \sum_j S(z_j - z_{is}^0) \left(\delta \mathbf{E}_j + \frac{\mathbf{v}_{is}^0 \times \delta \mathbf{B}_j}{c} \right)$$

$$= \frac{ie}{mc} \sum_{k,p} N_g S_{k_p} \int d\omega [(\omega - k v_{i\parallel}^0)\, \mathbf{A}_k(\omega) + k\hat{\mathbf{z}}(\mathbf{v}_{is} \cdot \mathbf{A}_k(\omega))]\, e^{ik_p z_i^0}$$

$$\times \exp[-i(\omega - k_p v_{i\parallel}^0)\, t], \tag{38}$$

where the Fourier transform of S is decomposed in its grid aliases (indexed by p) as

$$S(z) = \sum_{k'} \sum_p S_{k' + pk_g}\, e^{i(k' + pk_g)z} \tag{39}$$

and

$$\mathbf{A}_j(t) = \sum_k \int d\omega \mathbf{A}_k(\omega)\, e^{ikz_j - i\omega t}. \tag{40}$$

In the sums, k and k' take on the values $2\pi l/L$ for integers l between $-N_g/2 + 1$ and $N_g/2$, where L is the length of the system, while the alias index p runs from $-\infty$ to $+\infty$. We have also defined $k_p \equiv k + pk_g$ to be the pth alias wavenumber associated with wavenumber k, k_g being the grid wavenumber $2\pi N_g/L = 2\pi/\Delta z$.

Using the integrating factor $e^{i\Omega t}$, Eq. (38) yields

$$\delta v_{is}^+(t) = -\frac{e}{mc} \sum_{k,p} N_g\, S_{k_p} \int d\omega\, \frac{\omega - k v_{i\parallel}^0}{\omega - k_p v_{i\parallel}^0 - \Omega} A_k^+(\omega)\, e^{ik_p z_i^0}$$

$$\times \exp[-i(\omega - k_p v_{i\parallel}^0)\, t], \tag{41}$$

where $A^+ \equiv A_x + iA_y$ and $\delta v^+ \equiv \delta v_x + i\delta v_y$. In similar fashion, we obtain

$$\hat{\mathbf{x}}^- \cdot \sum_s \mathbf{v}_{is}^0(t)\, \delta z_{is}(t) = -\frac{ieN_s}{mc} \sum_{k,p} N_g\, S_{k_p} \int d\omega\, \frac{(1/2)\, k(v_{i\perp}^0)^2}{(\omega - k_p\, v_{i\parallel}^0 - \Omega)^2}\, A_k^+(\omega)\, e^{ik_p z_i^0} \times \exp[-i(\omega - k_p\, v_{i\parallel}^0)\, t], \tag{42}$$

by assuming

$$\sum_{s=1}^{N_s} e^{-2i\theta_{is}^0} = 0,$$

which holds when each group i is composed of at least three particles uniformly loaded in gyrophase space. (The four-spokes distributions used in our simulations have four uniformly loaded particles per group.) Here $\hat{\mathbf{x}}^- = (\hat{\mathbf{x}}^+)^* = \hat{\mathbf{x}} + i\hat{\mathbf{y}}$ is the basis vector dual to $\hat{\mathbf{x}}^+ \equiv \hat{\mathbf{x}} - i\hat{\mathbf{y}}$. Terms involving the constants of integration have been discarded in these expressions, since AIC-unstable time-Fourier components in the integral will eventually dominate. Substituting Eqs. (41) and (42) into the $(+)$ component of the linear current in Eq. (27), Fourier transforming the [illegible] the desired dispersion relation

$$D_0(k', \omega')\, A_{k'}^+(\omega') = -\frac{N_s}{N} \sum_{i,p} {\sum_{k',p'}}' D_1(k, k', p, p', \mathbf{v}_i^0, \omega') A_k^+(\omega_i)\, e^{i(k_p - k_p')z_i^0}, \tag{43}$$

where

$$D_0(k, \omega) \equiv \frac{k^2 v_A^2}{\Omega^2} + \frac{\omega}{\Omega} + \frac{N_s}{N} \sum_{i,p} N_g^2\, S_{k_p}^2 \left(\frac{\omega - k v_{i\parallel}^0}{\omega - k_p\, v_{i\parallel}^0 - \Omega} + \frac{(1/2)\, k k_p (v_{i\perp}^0)^2}{(\omega - k_p\, v_{i\parallel}^0 - \Omega)^2} \right) \tag{44}$$

is just the continuous-distribution dispersion function, including grid aliasing effects (cf. Ref. [31]),

$$D_1(k, k', p, p', \mathbf{v}_i^0, \omega') \equiv N_g^2 S_{k_p'} S_{k_p} \left(\frac{\omega_i - k v_{i\parallel}^0}{\omega_i - k_p v_{i\parallel}^0 - \Omega} + \frac{(1/2)\, k k_p' (v_{i\perp}^0)^2}{(\omega_i - k_p\, v_{i\parallel}^0 - \Omega)^2} \right), \tag{45}$$

$$\omega_i \equiv \omega' + (k_p - k_p')\, v_{i\parallel}^0, \tag{46}$$

and $k_p' \equiv k' + p' k_g$. The sum over k' and p' in Eq. (43) is meant to exclude those terms for which both $k' = k$ and $p' = p$.

The coupling process may be diagnosed by assuming the coupling and aliasing effects are weak and formally expanding Eq. (43) in orders of $(N/N_s)^{-1}$. (The actual expansion parameter is not in general $(N/N_s)^{-1}$ but depends on the statistics of how the particles were loaded. For example, if the particles were randomly loaded,

the expansion parameter may be expected to be of the form a constant times $(N/N_s)^{-1/2}$. The constant will usually be appreciably greater than one, since typically the resonant particles dominate the sum over i in Eq. (43) and thus effectively prevent the larger number of non-resonant particles from contributing to the statistics.)

The effects are most clearly illustrated by considering the coupling from a single "pump" wave with designated wavenumber and frequency k_0 and ω_0. The only equation that survives to zero-order in $(N/N_s)^{-1}$ is the k_0 component of Eq. (43),

$$D_0(k_0, \omega_0)\, A^+_{k_0}(\omega_0) = 0, \tag{47}$$

which simply indicates the pump wave must satisfy the uniform, grid-aliased, linear dispersion relation to zero-order. The $k' \neq k$ and/or $p' \neq p$ equations (coupling equations) first appear at first order:

$$A^+_{k'}(\omega') = -\frac{N_s}{N} \frac{D_1(k_0, k', p, p', \mathbf{v}_i^0, \omega_0)}{D_0(k', \omega')} A^+_{k_0}(\omega_0) \exp\{i[(k_0 + pk_g) - (k' + p'k_g)]\, z_i^0\}. \tag{48}$$

There is one equation and therefore one scattered wave for each combination of $k' \neq k_0$, $p' \neq p$, and particle group i. Since here $\omega_i = \omega_0$, the frequency of the wave scattered off particle group i to wavenumber k' through grid aliases p and p' is just

$$\omega' = \omega_0 - [(k_0 + pk_g) - (k' + p'k_g)]\, v^0_{i\parallel}. \tag{49}$$

Additional characteristics of linear scattering are revealed by considering under what circumstances scattering as described by Eq. (48) is most efficient. Scattering will generally be strongest when the effective coupling coefficient, D_1/D_0, is largest. Peaks in the magnitude of D_1/D_0 typically occur when two conditions are satisfied: (1) the particle group i off which scattering is to occur sees the Doppler-shifted pump wave frequency as the ion-cyclotron frequency, and (2) the daughter wave is (or is close to) an eigenmode of the system. The first condition derives from the resonant denominators in the expression for D_1 in Eq. (45) and demonstrates the requirement that there exist some particle group(s) i with parallel velocity

$$v^0_{i\parallel} \approx \frac{\omega_0 - \Omega}{k_0 + pk_g}, \tag{50}$$

for some integer p for a wave with frequency ω_0 and wavenumber k_0 to be linearly scattered. The second condition expresses the reasonable contention that the scattered wave satisfy

$$D_0(\omega', k') \approx 0. \tag{51}$$

The relationship between the pump wave and the daughter wave may be displayed geometrically. If the parallel velocity of the scattering particle group given by Eq. (50) is used in Eq. (49), we obtain the proportionality

$$\frac{\omega' - \omega_0}{(k_0 + pk_g) - (k' + p'k_g)} \approx \frac{\Omega - \omega_0}{k_0 + pk_g}, \tag{52}$$

illustrated in Fig. 6. Points representing the frequency and alias wavenumber of the two waves lie on (or near) a line having slope the parallel velocity $v_{i\|}^0$ passing through the point $(\Omega, 0)$. As indicated by Eqs. (47) and (51), the frequency of each wave will satisfy the zero-order dispersion relation at the *unaliased* wavenumber; thus each will reside on (or near) one of its branches.

Linear scattering is also governed by the statistics of the particle distribution through the complex exponential appearing in Eq. (48). If particle groups are randomly loaded, the exponential introduces a random direction in complex space, so that the sum of scattered waves may be loosely thought of as a series of random walks in complex space with step size the scattering coefficient. Thus we expect the amplitudes of scattered waves to scale as $(N/N_s)^{-1/2}$, as suggested earlier. If, on the other hand, the particles have been loaded in an organized manner; specifically, if particles are loaded uniformly in space for each $(v_\perp, v_z)$-pair appearing in the ion distribution, then the characteristics of linear scattering are changed and may then be described as aliasing off the spatial "grid" of particles.

Equations (47), (49), (50), and (51) along with the particle statistics introduced in Eq. (48) form, in brief, a set of laws applicable to the weak linear scattering process in simulations of parallel-propagating transverse waves in the ion-cyclotron frequency range. The discrepancies with uniform theory touched upon earlier now serve as examples of these laws.

In Figs. 4(a) through 4(c), we observe disproportionately high growth rates for the four highest modes kept by the simulation, modes 22 through 25. This behavior is easily shown to be the particle aliasing effect. Since the scattering coefficient is the

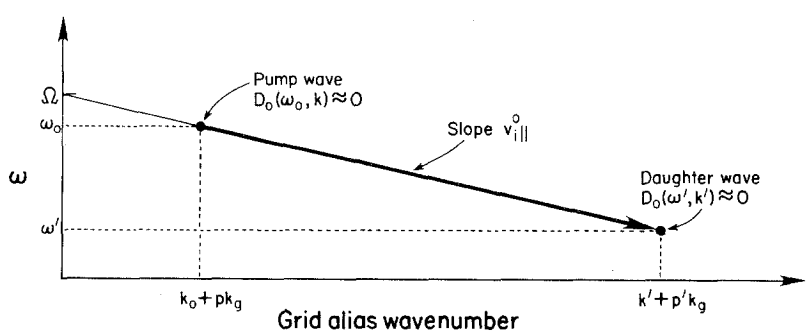

FIG. 6. Geometric relationship between the pump wave and the daughter wave in the linear scattering process in AIC simulations.

same for all particle groups in each beam, the complex exponential in Eq. (48) will cause the net scattering from each beam to sum to zero provided (1) the difference between the pump wave and daughter wave mode numbers is less than the number of particle groups, N_b, comprising each beam, and (2) the spatial distribution of particles in the beams is uniform. When the difference in mode numbers is a multiple of N_b, which, in this case is 47, the scattered waves combine constructively, and substantial mode coupling can result. Runs with different values of N_b verified that particle aliasing was indeed the operative agent. When $N_b = 44$, modes 19 through 25 showed enhanced growth. When $N_b = 51$, no enhanced growth was observed. The enhanced growth rate itself is explained by the strength of the coupling which, for these short-wavelength modes, tends to be strong. Thus the weak coupling approximation is not strictly correct, and the growth rates are determined by the fully coupled equations. The enhanced growth rate is not observed in Figs. 4(d) and (e), where the large number of beams presumably weakens the coupling.

In contrast, the whistler frequencies observed at short wavelengths modes (Fig. 5(a)) may be understood as a grid-aliasing effect. As shown in Fig. 7, one-beam modes whose resonant parallel velocities have the correct slopes may couple to alias whistler modes in the next Brillouin zone, producing the added peak in the frequency spectrum in the whistler frequency range seen in the typical spectrum displayed in Fig. 5(b). Similar coupling to one-beam modes, indicated by the dotted line in Fig. 7, is technically possible, but is not usually observed. The variation of the dispersion function D_0, $\partial D_0/\partial\omega$, in the vicinity of roots corresponding to the one-beam modes, is quite large ($\sim(1/\Omega)(kv_A/\Omega)^2(v_A/v_\perp)$) compared to the whistler

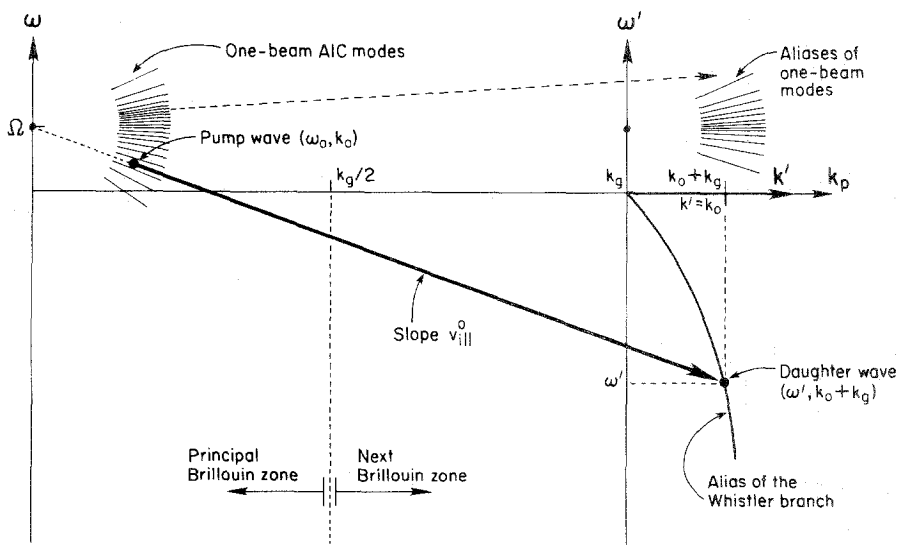

FIG. 7. Schematic of linear scattering of a one-beam AIC mode to a grid alias of the whistler mode. (Not drawn to scale.)

mode ($\sim(1/\Omega)$), The one-beam modes are thus "hard to find" and grid-induced scattering couples predominantly to the whistler.

A third example of linear mode coupling involves both wave-particle scattering and grid aliasing. The presence of "ghost peaks" in Figs. 4(d) and (e) may be explained by the coupling scheme shown in Fig. 8. Coupling may only occur to the specified points along the line of scattering. The separation of the points is $2\pi(47)/L$, since there are 47 particle groups in each beam. Most of these points do not participate in the coupling because either they are far from the normal modes of the system (point labeled "A") or they fall at high wavenumbers not followed by the simulation (points labeled "B"). However, when the pump wave is mode 4, the point marked "C" corresponds to mode 239 which, *modulo* 256 is mode (-17), a simulated mode of the system. Point "C" lies near the alias of the whistler branch, so we expect to see coupling of mode 4 to this mode. Since mode 4 is the fastest growing uncoupled mode of the system, mode (-17) should be the fastest growing of the waves linearly coupled in this fashion. This explains the ghost peak centered at mode 17 in Figs. 4(d) and (e) which we observe has the same height as the principal peak. We note also that no such peak is observed at mode 25 which corresponds to the alias of point "A" in Fig. 8. We can verify that ghost peaks occur by the mechanism described—when 46 particle groups are used per beam, ghost peaks occur at modes 22 and 24; when 45 groups are used, a peak occurs at mode 18—all as predicted by the theory.

The general characteristics of the linear behavior of multibeam distribution

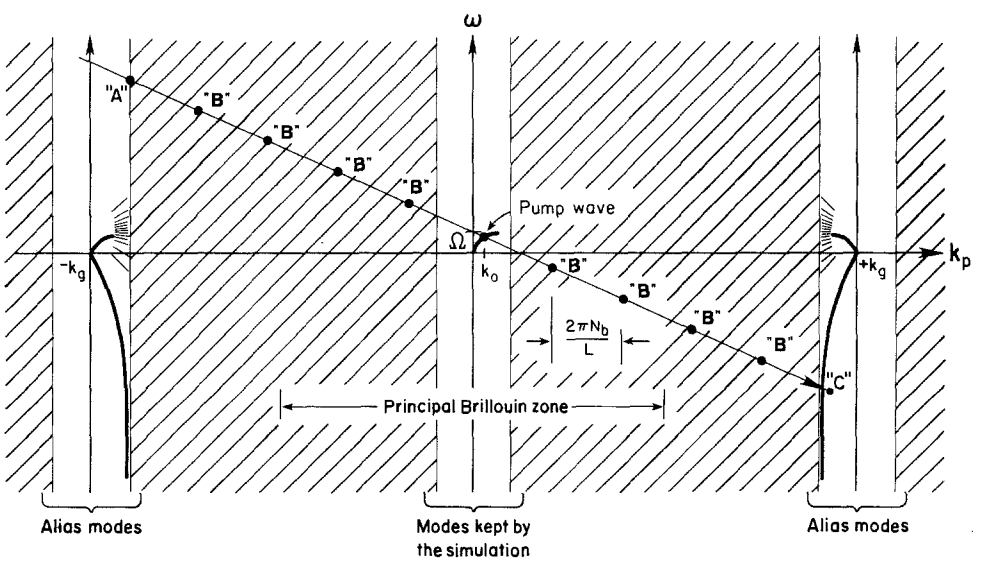

FIG. 8. Schematic of the coupling process responsible for the appearance of "ghost peaks" in the growth rate spectrum. Linear scattering couples the fastest growing waves in the principal Brillouin zone to whistler mode aliases. (Not drawn to scale.)

functions in simulation may be extended to the simulation of more realistic distributions such as the bimaxwellian distribution. The complicating feature here is that the number of values of $(v_\perp, v_\parallel)$ required to reasonably represent the bimaxwellian distribution is far too great to load in the form of beams. Instead, we represent each value of $(v_\perp, v_\parallel)$ with one particle group, and then scramble the positions of the groups in space using a base-3 variant of the usual bit-reversing algorithm. In essence, we are loading one particle group per beam. Equation (43) is therefore still valid in this sense, but there are no longer any selection rules; every mode is eligible to couple with every other.

The growth rates observed in a bimaxwellian simulation employing 16,384 particles is shown in Fig. 9(a). Most of the modes show growth rates substantially larger than the largest theoretical AIC growth rate, suggesting strong linear coupling as discussed earlier. When the number of particles is increased to 65,536 (Fig. 9(b)), the mode-coupled growth rates decrease and the characteristic peak of the AIC growth rate spectrum emerges. Characteristics of the mode coupling for this case may be determined from the mode histories shown in Fig. 10. These characteristics have been found to hold in general for all our AIC simulations.

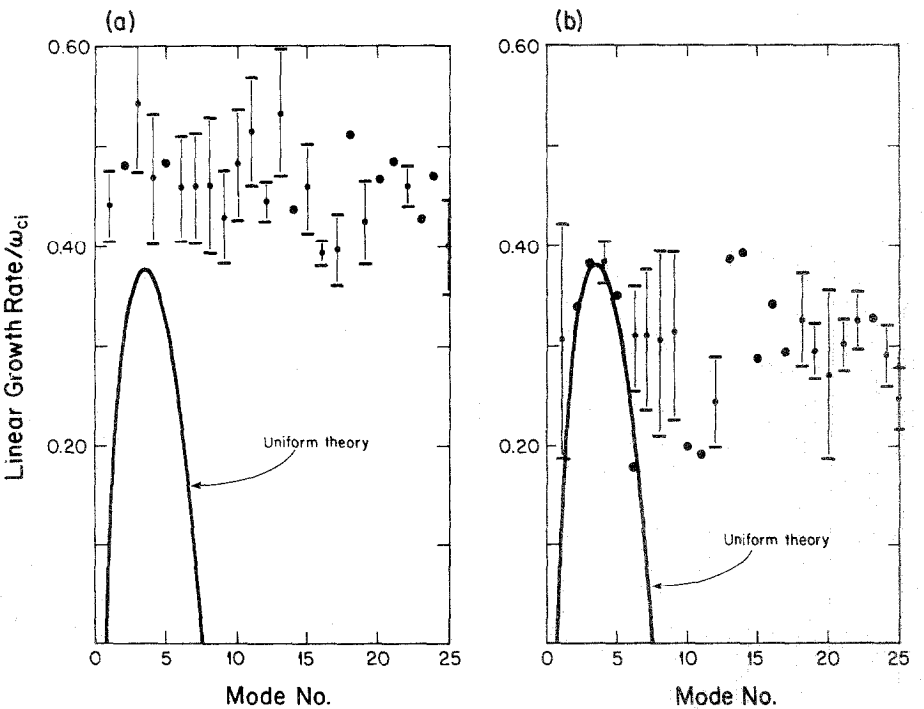

FIG. 9. Linear growth rates vs mode number obtained theoretically assuming a spatially uniform, bimaxwellian ion distribution function, and obtained from simulations using (a) 16,384 ions and (b) 65,536 ions. In both the theory and the simulations, $\beta_{i\perp} = 8$ and $T_{i\perp}/T_{i\parallel} = 4$. Simulation parameters were $\Delta t = 0.038\omega_{ci}^{-1}$, $N_g = 256$, and $\Delta z = 0.124 v_A/\omega_{ci}$.

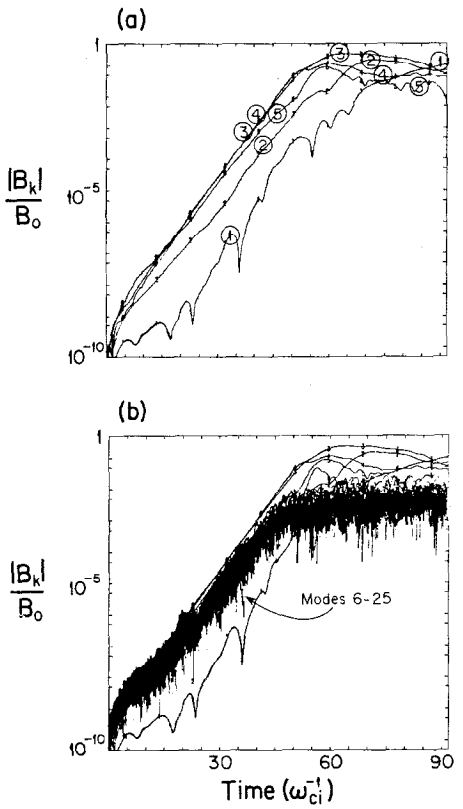

FIG. 10. Simulation wave magnetic field mode histories for a run employing a bimaxwellian distribution with $\beta_{i\perp} = 8$, $T_{i\perp}/T_{i\parallel} = 4$, 65,536 particles, $N_g = 256$, $\Delta t = 0.038\omega_{ci}^{-1}$, and $\Delta z = 0.124 v_A/\omega_{ci}$: (a) modes 1–5, (b) modes 6–25 with modes 1–5 shown for reference.

Modes composing the peak of the AIC growth spectrum, when present, always show clean exponential growth with growth rates very close to those predicted by theory (Fig. 10(a)). Modes to the long-wavelength side of the peak exhibit amplitudes well below those of the fastest growing modes, often grow exponentially at the low AIC growth rates predicted by theory, and generally appear to be only weakly coupled to other modes. In contrast, modes to the short-wavelength side of the peak tend to grow erratically, but taken as a group, grow at the same rate as the fastest growing mode in the system. The amplitudes of all the short-wavelength modes stay within a narrow range of each other throughout the linear stage, implying that the coupling among these modes is very tight; that is, the corresponding coupling coefficients in Eq. (48) are very large. The mode amplitudes as a group also stay within an order of magnitude of the fastest growing modes of the system, and as illustrated in Fig. 10(b), are often within a factor of two. This suggests that there is strong coupling of the fastest growing modes to short-wavelength modes as well.

The linear scattering scheme illustrated in Fig. 11 serves to explain this behavior. Each of the fan lines emanating from $(0, \Omega)$ represents by its slope one of the parallel velocities present in the distribution. As explained previously, mode coupling mediated by linear scattering is directed along these fan lines. We observe that the long-wavelength modes fall outside the thick of the fan and thus can participate at best weakly in the mode coupling process. Modes composing the peak of the AIC growth spectrum generally have the largest amplitude and therefore function primarily as pump waves. Since $\mathrm{Im}(\omega)$ is significant and positive for these modes, there will be significant coupling to available modes situated in some spread about the fan line on which the pump wave lies. Each effective pump wave may be thought of as a transmitter in $(\mathrm{Re}(\omega), k)$-space broadcasting with frequency $\mathrm{Re}(\omega)$ in (ω, k)-land with some radiation pattern whose details are determined by Eq. (45) and whose spread about the principal radiation directions is determined by the magnitude of $\mathrm{Im}(\omega)$. The radiation patterns are shown schematically in Fig. 11.

The best "receivers" (i.e., candidates for daughter waves) clearly lie to the short-wavelength side of each pump wave as illustrated in Fig. 11. Here the receivers are more in line with the pump waves in the peak of the AIC growth spectrum. Also, the slope of the short-wavelength portion of the AIC dispersion curve is close to the slopes of fan lines in its vicinity, implying the mode-coupling *among* the short-wavelength modes will tend to be tight. This effect tends to be augmented by the presence of the factor kk'_p in the last term in Eq. (45).

One worrisome consequence of strong mode coupling in the linear regime is observed in the case of a normal, Maxwellian distribution $(T_{i\perp}/T_{i\|} = 1)$. From the appearance of Fig. 9, it is perhaps not surprising that substantial and roughly

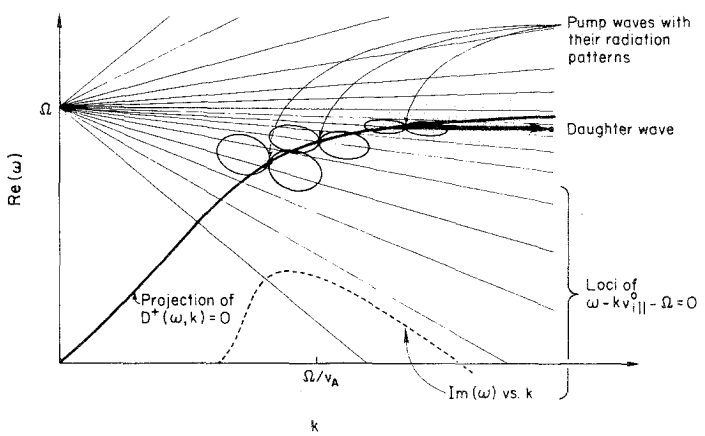

FIG. 11. Schematic of short-wavelength mode coupling. AIC-unstable modes on the Alfvén ion-cyclotron branch tend to linearly couple to other modes along fan lines determined by particle velocities present in the ion distribution function. Coupling is also significant along some spread of directions about the fan lines determined by the magnitude of $\mathrm{Im}(\omega)$, as indicated by the radiation patterns. Note that coupling by this mechanism involves primarily the short-wavelength modes.

comparable growth rates are observed for all the modes followed by the simulation, even for this theoretically stable case. We speculate that short-wavelength modes are being driven one-beam AIC unstable by beamlike structures in the fine structure of the initial distribution. Mode coupling then distributes the energy among the other longer wavelength modes, with the longest wavelengths showing only weak coupling, as evidenced by their comparatively small amplitudes. Figure 12 shows evidence of the coupling process. The four diagrams compare four of the modes of a multiwave $T_{i\perp}/T_{i\parallel} = 1$ simulation to four simulations, each of which kept only a single mode. All the growth rates of the multiwave simulation are comparable, while the single-wave simulations, which of course are not susceptable to mode coupling processes, show distinctly different growth rates for the different modes. Note also that the most unstable single-wave run was the one which followed the shortest wavelength, supporting the hypothesis that the one-beam AIC instability is the operative process.

The presence of these one-beam AIC instabilities may also cause problems in

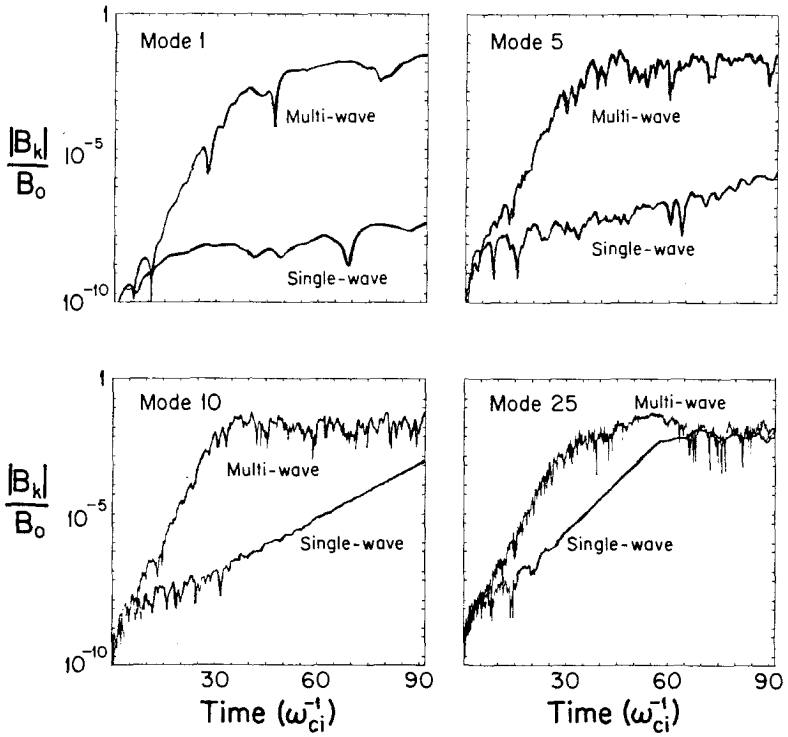

FIG. 12. Four simulations in which a single mode is kept are compared to a single simulation following the 25 lowest modes. Wave magnetic field histories are plotted for single mode runs keeping (a) mode 1, (b) mode 5, (c) mode 10, and (d) mode 25, along with the corresponding mode histories from the multi-mode run. In all the simulations, a Maxwellian distribution function was used ($T_{i\perp}/T_{i\parallel} = 1$) with $\beta_{i\perp} = 8$, 16,384 particles, $\Delta t = 0.038\omega_{ci}^{-1}$, $\Delta z = 0.124 v_A/\omega_{ci}$, and $N_g = 256$.

simulations of the nonlinear regime. The difficulties do not arise in most of our simulations, because the saturation levels of these short-wavelength instabilities typically lie one order of magnitude below the saturation levels of the principal AIC-unstable modes (for $\sim 10{,}000$ particles). This is confirmed by comparing simulations which either kept or artificially killed the short-wavelength modes. Histories of the longer wavelengths are not identically reproduced in the nonlinear regime when the short-wavelength modes are absent, but neither are any significant qualitative differences observed. These difficulties are, however, potentially serious when the theoretically stable Maxwellian distribution is used. Researchers engaged in simulations involving such ion distributions may well be interested in physical effects having mode amplitudes smaller than those generated by these fine-structure AIC instabilities. Such effects would then be masked, rendering the simulation useless.

The details of the saturation levels of these short-wavelength modes are described in a separate report [32]. It is concluded the noise generated by these instabilities are of particular concern for two reasons. First, the noise levels are quite substantial, and are not particularly diminished when no anisotropy is present. Very little dependence of the magnetic field noise levels on $\beta_{i\parallel}$ is observed in simulations while the dependence of $\beta_{i\perp}$ and on the number of simulation particles N ($|B_k| \sim N^{-1/2}$) is found to be significant. Second, these noise levels should be present in a fairly wide class of simulations. The levels observed in the simulations were found to match those predicted by the test-particle theorem for a Maxwellian distribution which applies in this instance to any system admitting parallel-propagating transverse waves in the ion-cyclotron frequency range. These levels are the levels that would be present at thermodynamic equilibrium and thus will generally tend to occur by any available mechanism. The suspected mechanism in our case, the one-beam AIC instability, similarly requires little for its existence. It will occur in the same systems for which the noise-level theory is valid, provided additionally that beamlike structures are present in the particle representation of the ion velocity distribution function. This last requirement is apparently easily satisfied, since the instability occurs in the presence of our representation of a Maxwellian distribution, which was constructed with no special provisions using standard simulation techniques.

Finally, it is worth mentioning that two of the processes described here, linear scattering and the relaxation of fine structure free energy in the ion distribution function via one-beam AIC instabilities, are *physical* processes which can occur in real systems under the right conditions, and are only simulation artifacts here in the sense that relatively small numbers of particles are being used. Linear scattering is manifested simply as a contribution to the electromagnetic fluctuation spectrum. On the other hand, one-beam AIC instabilities can be a very important effect in a real plasma. Any structure sharply peaked in parallel velocity with sufficient perpendicular temperature appearing anywhere in the ion velocity distribution function will exhibit the instability. Thus, one-beam AIC instabilities comprise another collisionless relaxation mechanism for free energy in a velocity distribution function in addition to the familiar bump-on-tail instability.

VII. Conclusions

A 1 2/2-d magnetoinductive hybrid simulation code has been used to simulate, and study simulation properties of, the Alfvén ion-cyclotron instability. While the AIC instability is the particular subject of interest here, many of the comments and simulation procedures described apply equally well to general parallel-propagating Alfvén waves as well as to waves on the whistler (electron-cyclotron) branch.

The code was used to model a non-physical multibeam ion distribution function, and the results were compared to a uniform, analytic theory. The principal AIC growth spectrum and linear growth rates associated with "one-beam" AIC instabilities appeared clearly in both theory and simulation; however, discrepancies were also noted. It was shown subsequently that all the discrepancies could be explained by refining the linear dispersion theory to include discrete particle and finite grid effects. Behavior of more realistic bimaxwellian ion distributions in simulation could also be explained by the refined theory. In particular, positive linear growth observed in simulations of a normal Maxwellian found explanation in the theory. The mechanism involved, the collisionless relaxation of the distribution by the growth of one-beam AIC instabilities, is physical, and thus should be operative in real plasmas characterized by peaked structures in parallel velocity space. The saturation levels of the troublesome short-wavelength modes were observed to agree with expected theoretical fluctuation levels. The observed levels did not interfere with the AIC simulations conducted for this study, but may be important to other electromagnetic simulations admitting parallel-propagating waves.

The theory and test simulations suggest some simulation guidelines which have been supported by more realistic simulations presented elsewhere [32]. We have found that a predictor-corrector type algorithm is not needed for simulation of these types of waves if a two-timestep averaging procedure is performed at the beginning of the simulation. Good energy conservation properties can be achieved by using a Boris-mover-like algorithm in advancing the fields as well as the particles. The main linear growth characteristics (associated with the principal growth peak) are best reproduced by faithfully representing the $v_\perp$-$v_\parallel$ portion of the velocity distribution. This is most easily accomplished by employing a large number of particle groups and loading one group per beam. This loading scheme also minimizes linear mode coupling effects by minimizing the growth rates of beam modes and the strong coupling effects of the "particle grid." The linear theory suggests, however, that the θ portion of the velocity distribution need not be carefully represented for the case of a gyrophase-independent distribution. Each particle group need only have a minimum of three particles, equally spaced in gyrophase. It is probably best to scramble these particle gyrophases from one particle group to the next using, for example, a bit-reversing scheme, so that the velocity distribution is reasonably represented when the nonlinear regime is entered by the simulation.

ACKNOWLEDGMENTS

The author wishes to thank Professor C. K. Birdsall for his several ideas and numerous discussions concerning simulation of the AIC instability. We also wish to acknowledge helpful suggestions from Dr. J. A. Byers, Dr. B. I. Cohen, Dr. W. M. Nevins, and Dr. G. R. Smith on this subject. Computational facilities were provided by the National Magnetic Fusion Energy Computer Center. This work was supported by U.S. Department of Energy Contract DE-AT03-76ET53064.

REFERENCES

1. T. A. CASPER AND G. R. SMITH, *Phys. Rev. Lett.* **48**, 1015 (1982).
2. R. C. DAVIDSON AND J. M. OGDEN, *Phys. Fluids* **18**, 1045 (1975).
3. G. R. SMITH, W. M. NEVINS, AND W. M. SHARP, *Phys. Fluids* **27**, 2120 (1984).
4. B. H. MAUK AND R. L. MCPHERRON, *Phys. Fluids.* **23**, 2111 (1980).
5. J. M. CORNWALL, F. V. CORONITI, AND R. M. THORNE, *J. Geophys. Res.* **75**, 4699 (1970).
6. M. N. ROSENBLUTH, *Bull. Amer. Phys. Soc. II* **4**, 197 (1959).
7. R. Z. SAGDEEV AND V. D. SHAFRANOV, *Zh. Eksper. Teoret. Fiz.* **39**, 181 (1960) *SSoviet Phys. JETP* **12**, 130 (1961)).
8. J. E. SCHARER AND A. W. TRIVELPIECE, *Phys. Fluids* **10**, 591 (1967).
9. J. E. SCHARER, *Phys. Fluids* **10**, 652 (1967).
10. J. SCHARER, *Plasma Phys.* **11**, 1 (1969).
11. A. HASEGAWA, *Physics and Chemistry in Space Vol. 8* (Springer, New York, 1957). p. 79.
12. G. R. SMITH, *Phys. Fluids* **27**, 1499 (1984).
13. J. G. CORDEY AND R. J. HASTIE, *Phys. Fluids* **15**, 2291 (1972).
14. J. D. HANSON AND E. OTT, *Phys. Fluids* **27**, 150 (1984).
15. T. D. ROGNLIEN AND D. C. WATSON, *Phys. Fluids* **22**, 1958 (1979).
16. D. C. WATSON, *Phys. Fluids* **23**, 2485 (1980).
17. D. C. WATSON, R. J. FATEMAN, AND D. E. BALDWIN, *Phys. Fluids* **21**, 1657 (1978).
18. T. TAJIMA AND K. MIMA, *Phys. Fluids* **23**, 577 (1980).
19. R. Z. SAGDEEV AND A. A. GALEEV, *Nonlinear Plasma Theory*, edited by T. M. O'Neil and D. L. Book (Benjamin, New York, 1969).
20. S. L. OSSAKOW, E. OTT, AND I. HABER, *Phys. Fluids* **15**, 2314 (1972).
21. R. M. THORNE, *Rev. Geophys. Space Phys.* **13**, 291 (1975).
22. A. HASEGAWA AND C. K. BIRDSALL, *Phys. Fluids* **7**, 1590 (1964).
23. S. CUPERMAN, A. STERNLIEB, AND D. J. WILLIAMS, *J. Plasma Phys.* **16**, 57 (1976).
24. T. TAJIMA AND J. M. DAWSON, *Nucl. Fusion* **20**, 1129 (1980).
25. J. AMBROSIANO AND S. H. BRECHT, *Phys. Fluids*, in press.
26. J. A. BYERS, *Phys. Rev. Lett.* **39**, 1476 (1977).
27. J. A. BYERS, B. I. COHEN, W. C. CONDIT, AND J. D. HANSON, *J. Comput. Phys.* **27**, 363 (1978).
28. J. P. BORIS, in *Proceedings, Fourth Conference on Numerical Simulation of Plasmas*, edited by J. P. Boris and R. Shanny (U.S. Government Printing Office, Washington, D.C., 1970), p. 3.
29. C. K. BIRDSALL AND A. B. LANGDON, *Plasma Physics via Computer Simulation* (McGraw–Hill, New York, 1985), p. 20.
30. B. I. COHEN, T. A. BRENGLE, D. B. CONLEY, AND R. P. FREIS, *J. Comput. Phys.* **38**, 45 (1980).
31. C. K. BIRDSALL AND A. B. LANGDON, *Plasma Physics via Computer Simulation* (McGraw–Hill, New York, 1985), Chap. 8.
32. N. F. OTANI, Phys. Fluids, in press.